

1  
2  
3  
4  
5  
6  
7  
8  
9  
10  
11  
12  
13  
14  
15  
16  
17  
18  
19  
20  
21  
22  
23

# **Quantitative prediction of ensemble dynamics, shapes and contact propensities of intrinsically disordered proteins**

Lei Yu<sup>1</sup> and Rafael Brüschweiler<sup>1,2\*</sup>

<sup>1</sup>Department of Chemistry and Biochemistry, The Ohio State University, Columbus, Ohio, United States of America

<sup>2</sup>Department of Biological Chemistry and Pharmacology, The Ohio State University, Columbus, Ohio, United States of America

\* Corresponding author

E-mail: [bruschweiler.1@osu.edu](mailto:bruschweiler.1@osu.edu) (RB)

Short title: “Quantitative prediction of structural dynamics of IDPs”

24 **ABSTRACT**

25 Intrinsically disordered proteins (IDPs) are highly dynamic systems that play an important role in  
26 cell signaling processes and their misfunction often causes human disease. Proper understanding  
27 of IDP function not only requires the realistic characterization of their three-dimensional  
28 conformational ensembles at atomic-level resolution but also of the time scales of  
29 interconversion between their conformational substates. Large sets of experimental data are often  
30 used in combination with molecular modeling to restrain or bias models to improve agreement  
31 with experiment. It is shown here for the N-terminal transactivation domain of p53 (p53TAD)  
32 and Pup how the latest advancements in molecular dynamics (MD) simulations methodology  
33 produces native conformational ensembles by combining replica exchange with series of  
34 microsecond MD simulations. They closely reproduce experimental data at the global  
35 conformational ensemble level, in terms of the distribution properties of the radius of gyration  
36 tensor, and at the local level, in terms of NMR properties including  $^{15}\text{N}$  spin relaxation, without  
37 the need for reweighting. The IDP ensembles were analyzed by graph theory to identify  
38 dominant inter-residue contact clusters and characteristic amino-acid contact propensities. These  
39 findings indicate that modern MD force fields with residue-specific backbone potentials can  
40 produce highly realistic IDP ensembles sampling a hierarchy of nano- and picosecond time  
41 scales providing new insights into their biological function.

42

43

44 **AUTHOR SUMMARY**

45 Accurate prediction of the conformational ensemble dynamics sans bias is shown for intrinsically  
46 disordered proteins including the transactivation domain of p53.

47

## 48 INTRODUCTION

49 Intrinsically disordered proteins (IDPs) and protein regions (IDRs) are an integral part of the  
50 proteomes of many different organisms with more than 30% of all eukaryotic proteins possessing  
51 40 or more consecutive disordered residues.(1, 2) While IDPs and IDRs in isolation do not adopt  
52 well-defined three-dimensional (3D) structures, they often play important biological roles in  
53 molecular recognition processes by interacting in specific ways with binding partners that are  
54 typically well-ordered.(3-5) For instance, the human oncoprotein protein p53 possesses the N-  
55 terminal transactivation domain (p53TAD) that binds to the N-terminal domain of human  
56 MDM2 protein adopting a stable  $\alpha$ -helix.(6) Prokaryotic ubiquitin-like protein (Pup) is another  
57 IDP that is directly linked to protein degradation folding into an  $\alpha$ -helix when binding to Mpa  
58 protein.(7) In addition to binding to their target protein(s), IDPs can also be involved in liquid-  
59 liquid phase separation (LLPS).(8-11) LLPS is the segregation of molecules in solution into a  
60 condensed phase and a dilute phase with high and low biomolecular concentrations. These  
61 membraneless droplet-like compartments formed by IDPs and other biomolecules are important  
62 for cellular function. Knowledge of the structural and dynamic propensities of IDPs both in  
63 isolation and in complex biological environments is essential for understanding these processes  
64 and their role in human diseases.

65 In order to relate IDP sequences to biological function, detailed knowledge of IDP  
66 conformational ensembles is needed. The description of conformational ensembles can range  
67 from local secondary structure populations to explicit ensembles in 3D space with atomic  
68 resolution.(12) Some of the earliest approaches generate random coil conformational ensembles  
69 that are subsequently refined against a host of experimental data reflecting both local and global  
70 structural features.(13-15) These approaches continue to be successfully applied through  
71 integrative modeling provided that a large amount of high quality experimental data is available  
72 for each system under investigation.(16, 17) Even when data from various complementary  
73 experimental techniques are being used, the amount of experimental information obtainable is  
74 still sparse when compared to the information needed to uniquely characterize large, highly  
75 heterogeneous structural ensembles that are the hallmark of IDPs. As a consequence, the amount  
76 of information that can be gained and that is not directly reflected in the experimental data used  
77 to refine the ensemble is restricted to robust descriptors ranging from coarse-grained to global

78 that can be compared with predictions by polymer theory under various assumptions.(16) In  
79 addition, site-specific interaction information, such as transient inter-residue contacts, can be  
80 obtained at medium to low resolution from paramagnetic relaxation enhancement (PRE)  
81 experiments by attaching electron spin labels to selected sites.(15, 17) Because empirical  
82 ensembles generated based on such data lack a time axis, they do not include dynamics time  
83 scales of IDPs associated with interconversion rates between substates and, hence, they do not  
84 inform about an essential part of the energy landscape.

85 From a theoretical and computational perspective, all-atom molecular dynamics (MD)  
86 simulations are an attractive alternative to empirical approaches for the generation of IDP  
87 conformational ensembles, including dynamic time scale information, for the comprehensive  
88 interpretation of experimental results.(18) However, for many years limitations in computer  
89 power precluded the generation of statistically well-converged results and MD force fields  
90 primarily developed for ordered proteins turned out to be unsatisfactory for applications to IDPs.  
91 With the continuing increase in computer power, the quality of sampling has reached a level that  
92 allows rigorous validation by quantitative comparison with a rich body of experimental data. In  
93 cases where discrepancies are observed between simulation and experiment, as is commonly the  
94 case, approaches have been developed that use restraining or reweighting that bias the original  
95 simulation to obtain results that agree better with experimental data.(19-26) When not only the  
96 conformational ensemble but also the underlying dynamics time scales are of interest, suitable  
97 rescaling of the MD time step or correlation times of the dominant motional modes can be  
98 applied to improve agreement with experiment.(27-30) Because these methods can often  
99 improve the unaltered simulations only within certain boundaries, they are best suited when the  
100 original predictions are fairly close to experimental data.(31) Although these methods rarely fail  
101 to produce better agreement, at least on average for those experimental parameters directly used  
102 as restraints or for reweighting, they naturally depend on large amounts of experimental data of  
103 good quality as input for each protein system studied. This amounts to a laborious experimental  
104 effort that needs to be repeated for each new protein system as the experimental data are protein-  
105 specific rendering them non-transferrable between systems.

106 An alternative and more principled approach is to improve the MD force fields  
107 themselves enabling them to increasingly accurately predict experimental data in a way that is

108 fully transferrable between protein systems, both ordered and disordered. This premise has led to  
109 a recent proliferation of protein force field developments(32-37) and new explicit water  
110 models(38-40) specifically geared toward the improved representation of disordered proteins. In  
111 a significant development, residue-specific force fields have been introduced.(41) These force  
112 fields use in addition coil library information from the Protein Data Bank (PDB) by  
113 incorporating the individual backbone  $\phi, \psi$  propensities of each residue type.(41-47) Such  
114 residue-specific force fields, in combination with suitable water models, can provide an  
115 improved representation of disordered states while retaining the properties of ordered proteins.  
116 With respect to water models, TIP4P-D and closely related derivatives have been notably  
117 successful in preventing overly compact conformations by favoring more extended IDP  
118 structures showing improved agreement with experiment.(38)

119 Besides global properties, such as the radii of gyration and asphericities, IDP ensembles  
120 and trajectories should also accurately reproduce local dihedral angle distributions and secondary  
121 structure propensities. Moreover, they should also replicate dynamic and kinetic IDP properties,  
122 such as librational motions and time scales of interconversion between conformational substates.  
123 Such information is important for understanding recognition events between IDPs and their  
124 binding targets, including IDP interactions with other disordered biomolecules, for example,  
125 during the formation of LLPS condensates. Experimental IDP dynamics information can be  
126 gained from fluorescence depolarization spectroscopy,(48) Förster resonance energy transfer  
127 (FRET),(16) and nuclear magnetic resonance (NMR) relaxation.(15) NMR  $^{15}\text{N}$  longitudinal  $R_1$   
128 and transverse  $R_2$  spin relaxation rates are exquisitely sensitive to the dynamics of disordered  
129 proteins and the underlying time scales.(49-51)  $R_2$  relaxation rates, for example, have been  
130 linked to residual intramolecular interactions in chemically unfolded proteins.(51-53)  $^{15}\text{N}$   $R_1$  and  
131  $R_2$  rates can be experimentally determined for each protein residue and therefore they are  
132 valuable for validating MD simulations with respect to amplitudes and time scales of IDP  
133 dynamics.(29, 54-56)

134 We recently developed the AMBER ff99SBnmr2 force field by modifying the backbone  
135 dihedral angle potentials of each amino-acid residue type to reproduce the  $\phi, \psi$  dihedral angle  
136 distributions found in a random coil library.(57) The ff99SBnmr2 force field has been validated  
137 against experimental nuclear magnetic resonance (NMR) scalar  $^3J$ -couplings of  $\alpha$ -synuclein and

138  $\beta$ -amyloid IDPs demonstrating that this force field accurately reproduces their sequence-  
139 dependent local backbone structural propensities.(58) The primary goal of this work is to learn  
140 whether state-of-the-art replica exchange and extended MD simulations of IDPs can also  
141 realistically reproduce NMR  $R_1$ ,  $R_2$  relaxation rates with their strong and unique dependence on  
142 motional time scales without the need of any additional corrections such as constraints or  
143 reweighting. Moreover, in-depth analysis of the MD trajectories generated yields a wealth of  
144 information about the radius of gyration tensor distribution and dominant dynamics modes  
145 allowing graph-theory based identification of specific inter-residue interaction propensities and  
146 residue clusters for the better understanding of IDP behavior.

## 147 RESULTS

148 **Ensemble properties of radius of gyration tensor.** The radius of gyration  $R_g(t)$  is shown as a  
149 function of time for representative 1- $\mu$ s MD trajectories of p53TAD and Pup in **Fig. 1A,B** (see  
150 also **Fig. S1**). The trajectories exhibit predominantly stationary stochastic behavior reflecting  
151 random expansion and contraction of the overall IDP size with the mean value (blue horizontal  
152 lines) in good agreement with the experimentally determined  $\langle R_g \rangle$  (black line) or the predicted  
153  $\langle R_g \rangle$  from polymer theory (**Eq. 6**). The MD-distributions of  $R_g$  of all 10 MD trajectories are  
154 shown as histograms in **Fig. 1C,D**. The Flory exponent  $\nu$  of the polymer scaling law was  
155 determined from the REMD ensembles at 298 K. Using  $\rho_0 = 1.927 \text{ \AA}$ , we obtain a value of  $\nu =$   
156 0.601 for Pup, which closely matches the theoretical value  $\nu_{\text{theory}} = 0.588$  of a fully disordered,  
157 self-avoiding random coil.(59, 60) For p53TAD, the  $\langle R_g \rangle$  value of 28.1  $\text{\AA}$  is in almost perfect  
158 agreement with experiment (28.0  $\text{\AA}$ ) corresponding to  $\nu = 0.624$ , which clearly exceeds  $\nu_{\text{theory}}$ .

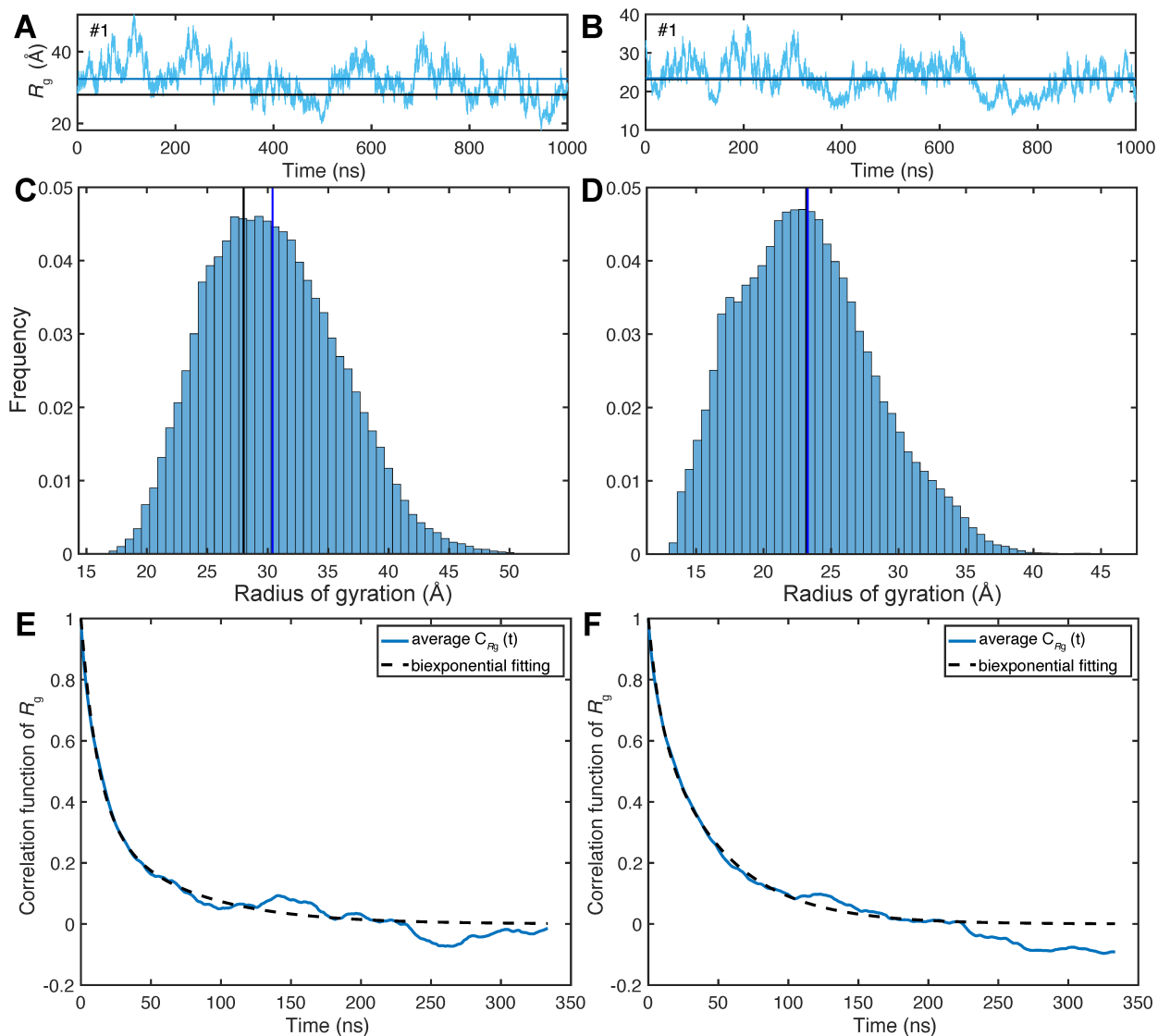
159

160

161

162

163



164

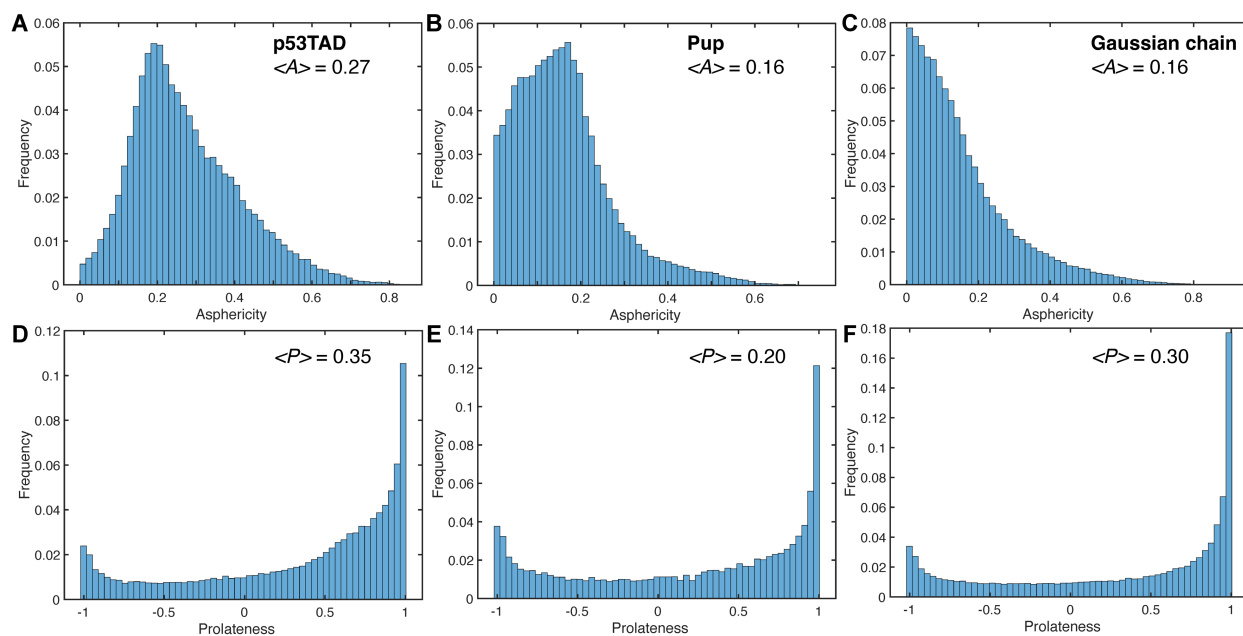
165 **Fig. 1.** Radius of gyration,  $R_g$ , properties of two IDPs p53TAD and Pup from microsecond MD  
 166 simulations. Time-dependence of  $R_g(t)$  from representative 1- $\mu$ s MD trajectories (cyan) of (A)  
 167 p53TAD and (B) Pup where the horizontal blue lines correspond to the mean  $R_g$  values  
 168 calculated from the trajectories and the black lines correspond to the experimentally determined  
 169  $R_g$  for p53TAD and the predicted  $R_g$  according to polymer theory for Pup.  $R_g$  profiles for all 10  
 170 1- $\mu$ s trajectories of each protein are shown in Figure S1. Histograms of the  $R_g(t)$  distributions  
 171 over all 10 MD simulations are shown in Panels C, D (blue and black lines have the same  
 172 meaning as in Panels A, B). The standard deviation of  $R_g$  over all 10 MD trajectories is 5.4 Å for  
 173 p53TAD and 5.0 Å for Pup. Offset-free time-correlation functions  $C_{R_g}(t)$  of  $R_g(t)$  averaged over  
 174 all 10 1- $\mu$ s MD trajectories are shown for (E) p53TAD and (F) Pup. The dashed lines belong to  
 175 non-linear least squares fits of  $C_{R_g}(t)$  by biexponential functions whereby the best fits are  
 176 obtained for p53TAD with  $\tau_a = 12$  ns (63% of total amplitude),  $\tau_b = 62$  ns (37%) and for Pup  
 177 with  $\tau_a = 8$  ns (29%),  $\tau_b = 48$  ns (71%).



178 The characteristic time scales of  $R_g(t)$  fluctuations can be obtained from the time-  
179 correlation functions  $C_{R_g}(t)$  (**Eq. 5**), which are well-converged over the course of the 1- $\mu$ s  
180 trajectories (**Fig. 1E,F**).  $C_{R_g}(t)$  of both proteins decay in good approximation biexponentially  
181 with reconfigurational correlation times  $\tau_a \approx 10$  ns and  $\tau_b \approx 55$  ns. The normalized variance of the  
182  $R_g(t)$  fluctuations, given by

$$183 \quad \sigma_{R_g}^2 = 1 - \frac{\langle R_g \rangle^2}{\langle R_g^2 \rangle} \quad (1)$$

184 is almost the same for p53TAD (0.03) and Pup (0.04). The ensemble distribution of the gyration  
185 tensor  $\mathcal{S}$  (**Eq. 2**) contains information about the deviation of individual MD snapshots from  
186 spherical shape, which can be directly compared with a random Gaussian chain serving as a  
187 perfect random coil (**Fig. 2**).<sup>(61)</sup> Both proteins show unimodal asphericity distributions (**Eq. 3**)  
188 with maxima around  $A \approx 0.18$ , which qualitatively differ from the Gaussian chain model (**Fig. 2C**)  
189 peaking at  $A = 0$ . Compared to p53TAD, Pup has a higher tendency to adopt a more spherical  
190 conformation. Another useful measure of the overall shape of individual snapshots is the  
191 prolateness  $P$  (**Eq. 4**). The distribution of  $P$  is bimodal for both proteins with the global  
192 maximum corresponding to prolate-shaped (cigar-like) structures ( $P = 1$ ) and a second (local)  
193 maximum corresponding to disk-like structures ( $P = -1$ ). The distribution of the prolateness of  
194 Pup is more balanced between positive and negative values with  $\langle P \rangle = 0.2$  than for p53TAD,  
195 which has a higher tendency to adopt prolate-shaped conformers ( $\langle P \rangle = 0.35$ ), whereas the  
196 Gaussian chain distribution ( $\langle P \rangle = 0.3$ ) lies between the two IDP distributions. The distinct  
197 asphericity distribution and increased prolateness of p53TAD is at the origin of its increased  $\langle R_g \rangle$   
198 over the Gaussian random coil model.



199

200

201 **Fig. 2.** Gyration tensor properties of IDP ensembles of p53TAD and Pup across 10 1- $\mu$ s MD  
 202 trajectories. The distributions of gyration tensor asphericities  $A$  are shown for (A) p53TAD and (B)  
 203 Pup in comparison with (C) a Gaussian chain. The distributions of gyration tensor prolateness  $P$   
 204 are shown for (D) p53TAD and (E) Pup in comparison with a (F) Gaussian chain.

205

206 **Validation against  $R_1$ ,  $R_2$  relaxation data.** Experimental and computed  $^{15}\text{N}$   $R_1$ ,  $R_2$  relaxation  
 207 rates are shown in **Fig. 3**.  $R_1$  relaxation rates determined from simulations (**Eq. 7–12**) are in close  
 208 agreement with experiment evidenced by small RMSEs ( $0.10 \text{ s}^{-1}$  for p53TAD and  $0.12 \text{ s}^{-1}$  for  
 209 Pup) and Pearson correlation coefficients  $R$  of 0.78 for p53TAD and 0.86 for Pup (**Fig. 3A,B**).  
 210  $R_2$  relaxation rates determined from the simulations are also in good agreement with experiment  
 211 with correlation coefficients  $R$  of 0.88 for p53TAD and 0.70 for Pup and RMSEs of  $0.84 \text{ s}^{-1}$  for  
 212 p53TAD and  $0.81 \text{ s}^{-1}$  for Pup and (**Fig. 3C,D**). It can be seen that the simulations tend to  
 213 underestimate  $R_1$  and overestimate  $R_2$  rates, although only slightly, in a manner that is notably  
 214 uniform for the  $R_1$  values of both proteins and for the  $R_2$  values of p53TAD. The 10 N-terminal  
 215 residues of p53TAD are very flexible with small  $R_2$ 's, which closely follow the experiment. For  
 216 Pup, differences in  $R_2$  between MD and experiment display the same trend and are most  
 217 pronounced for residues 30–48. The error bars of the computed relaxation rates, which represent  
 218 the root-mean-square deviations over all 10 MD trajectories, are fairly uniform along the  
 219 polypeptide chains and systematically larger for  $R_2$  than for  $R_1$ , again with the exception of the

220 10 N-terminal residues of p53TAD. For both proteins, not all 10 1- $\mu$ s MD trajectories  
221 individually reproduce the experimental data equally well. Either 1 (p53TAD) or 2 (Pup)  
222 trajectories have more compact average IDP structures, which quantitatively affect the agreement  
223 with experiment (**Fig. S2**).

224 Correlation times of backbone N-H bond vectors in both proteins fitted from the average  
225 correlation functions range from picoseconds to about 20 ns (**Fig. 3E,F**). Consistent with the  
226 finding for other IDPs,(55, 62) the dominant contribution to the time correlation functions stems  
227 from dynamics on the intermediate time scale around 1 ns reporting about backbone  $\phi,\psi$  jumps.  
228 Fast dynamics on the time scale of 100 ps or faster report on local  $^{15}\text{N}$ - $^1\text{H}$  bond librations, similar  
229 to those observed in secondary structures of folded proteins,(63) and slower dynamics on the  
230 time scale between 3 and 20 ns reports on collective IDP chain motions. The presence of slower  
231 modes correlate with increased  $R_2$  values most pronounced for residues 30–48 in Pup. This is  
232 consistent with relaxation theory (**Eq. 12**), which predicts that in solution transverse spin  
233 relaxation rates  $R_2$  are in good approximation proportional to the effective overall correlation  
234 time experienced by the  $^{15}\text{N}$ - $^1\text{H}$  spin pairs.

235

236

237

238

239

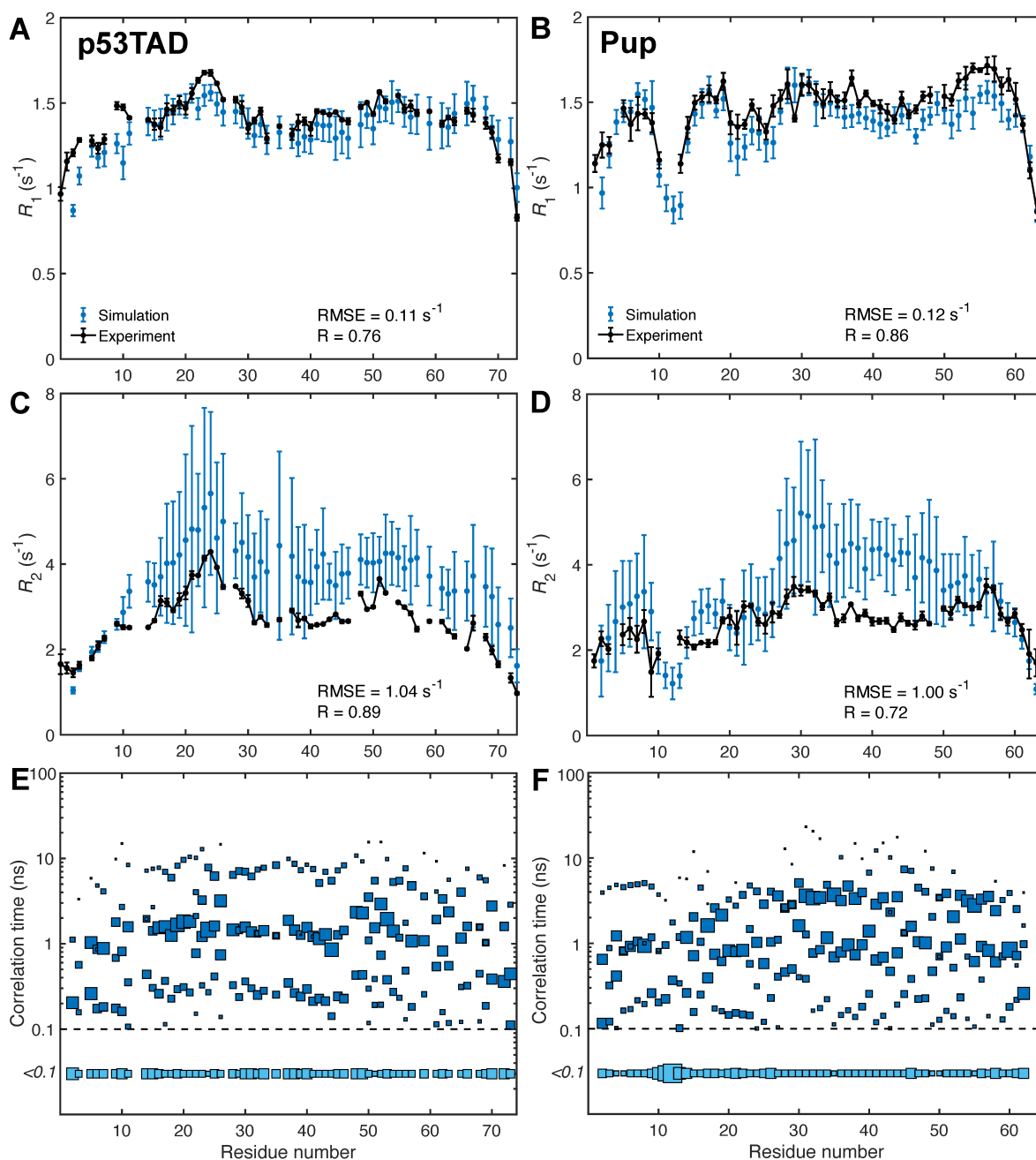
240

241

242

243

244



245

246 **Fig. 3.** Back-calculated  $R_1$ ,  $R_2$  NMR  $^{15}N$ -spin relaxation rates in comparison with experiment  
 247 along with underlying motional time scale distributions.  $R_1$ ,  $R_2$  rates calculated from average  
 248 correlation functions are plotted in blue with error bars representing standard deviations across  
 249 individual MD trajectories. Correlation time distribution of individual  $^{15}N$ - $^1H$  bonds of IDPs  
 250 extracted from correlation functions for (E) p53TAD and (F) Pup where the size of the blue  
 251 squares are proportional to the associated motional amplitudes  $A_i$ . The squares at the bottom  
 252 indicate the aggregate of dynamics contributions with correlation times faster than 100 ps.  
 253 Dominant dynamics time scales range from about 100 ps to about 10 ns depending on the residue,  
 254 with the exception of Thr12 in Pup which exhibits dominant dynamics time scales faster than  
 255 100 ps.

256 Increased transverse NMR spin relaxation is indicative of the presence of collective  
257 segmental motions in IDPs, which are modulated by the formation of transient secondary  
258 structures and inter-residue side-chain interactions. To examine these relationships,  
259 instantaneous secondary structures and average contact maps were determined from the MD  
260 trajectories (**Fig. 4**). A contact is defined in an MD snapshot when the nearest distance between  
261 atoms from two different residues is smaller than 4 Å (uninformative first-neighbor ( $i,i+1$ ) and  
262 second-neighbor ( $i,i+2$ ) contacts between residues were excluded (white band along diagonal in  
263 **Fig. 4A,B**). The most frequent contacts are relatively short range, but contacts over larger  
264 distances occur for p53TAD and even more frequently for Pup. Some contacts are linked to the  
265 transient formation of short secondary structures,  $\alpha$ -helices and  $\beta$ -strands (**Fig. 4C,D**), whereas  
266 other regions display frequent contacts largely independent of secondary structure propensity  
267 often involving arginine residues, such as Arg65 of p53TAD and Arg28/29 and Arg56 of Pup.  
268 **Fig. 4C,D** also shows that selected trajectories possess regions with well above-average  
269 secondary structure propensities, such as trajectories #4 of p53TAD and trajectories #5 and #7 of  
270 Pup, which are the same trajectories that contribute to the lengthening of  $R_2$  along parts of the  
271 polypeptide sequences mentioned above. Due to their atypical nature, not representative of the  
272 other trajectories, they were excluded for some of the following residue-cluster analysis. For  
273 p53TAD, regions that tend to form  $\alpha$ -helices do not form  $\beta$ -strands and vice versa (except for  
274 trajectory #4). For Pup, on the other hand, a number of regions exist in its N-terminal half that  
275 can transiently switch between these two types of local secondary structures.

276

277

278

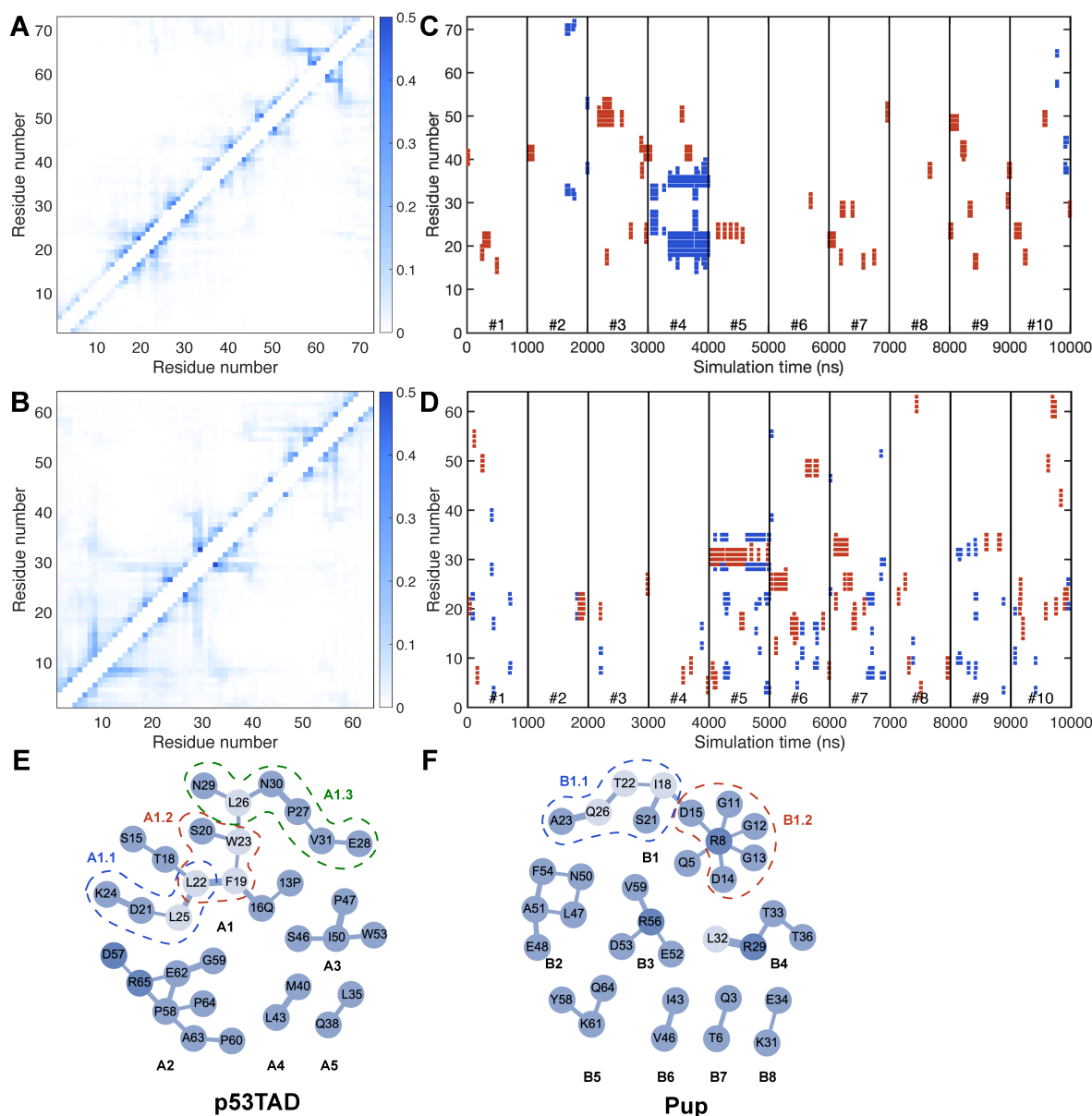
279

280

281

282

283



284

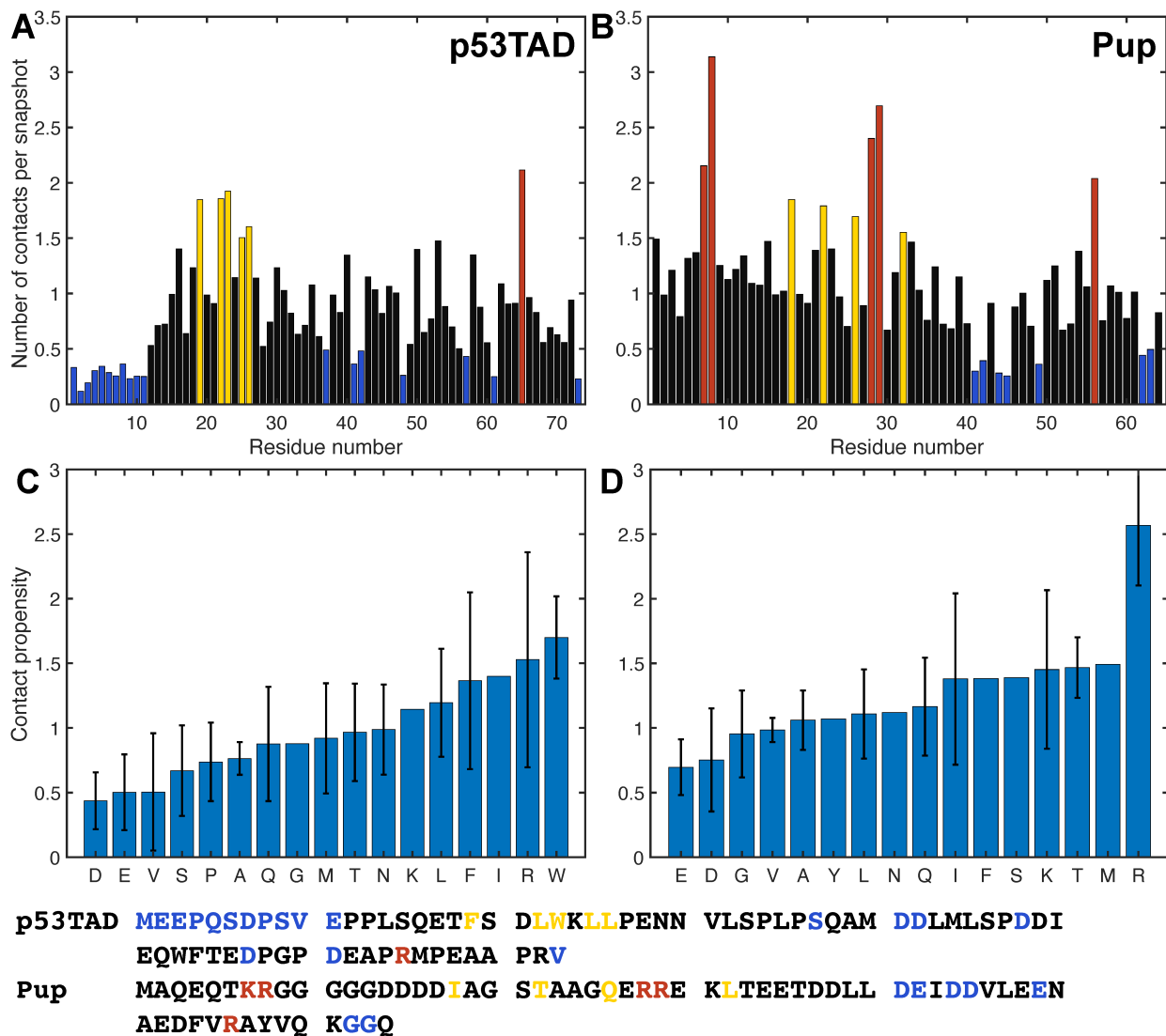
285 **Fig. 4.** Average IDP contact maps and time-dependent secondary structure formation of each  
 286 residue. (A, B) Pairwise contact occupancies were determined from MD simulations (without  
 287 atypical trajectories, **Fig. S2**) for (A) p53TAD and (B) Pup. Darker/lighter shades of blue denote  
 288 contacts that are more frequently/rarely formed according to legend (vertical bar). Self-contacts,  
 289 first-neighbor contacts (between residues  $i, i+1$ ), and second-neighbor contacts (between residues  
 290  $i, i+2$ ) are not shown since they are present in most snapshots. (C, D) secondary structure of each  
 291 residue in MD simulations are predicted using the DSSP algorithm with  $\alpha$ -helices shown in red  
 292 and  $\beta$ -strands in blue. (E, F) In the residue clusters at the bottom, pairwise contacts with  
 293 occupancies  $> 0.2$  are depicted as an edge connecting two nodes (residues) with edge widths  
 294 proportional to the pairwise contact occupancies. Labels A1–A5 denote dominant clusters in  
 295 p53TAD and B1–B8 in Pup. Examples of transiently formed subclusters are indicated by dashed  
 296 lines (A1.1, A1.2, and A1.3 in p53TAD and B1.1 and B1.2 in Pup).

297 **Inter-residue contact propensities.** Different residues along the polypeptide chain display  
298 different tendencies to form contacts with other residues. **Fig. 5A,B** shows the average number  
299 of contacts per snapshot for each residue, which was calculated as the total number of contacts  
300 formed by a residue divided by the total number of MD snapshots. To better visualize the  
301 different behaviors, the residues were divided into four distinct groups: the majority of residues  
302 that form 0.5–1.5 contacts per snapshot (colored in black), residues that form an unusually small  
303 number of contacts ( $< 0.5$ ) (colored in blue), residues that form a moderately large number of  
304 contacts (1.5–2) (colored in yellow), and residues that form a relatively large number of contacts  
305 ( $> 2$ ) are colored in red. For Pup, there are three distinct regions that form the largest numbers of  
306 contacts (red) comprising residues (1) Lys7, Arg8, (2) Arg28, Arg29, and (3) Arg56. They  
307 perfectly align with the three centers of **Fig. 3** with elevated  $R_2$  values, namely (1) Arg8, (2)  
308 Arg29, and (3) Arg56. For p53TAD, the residue that forms the largest number of contacts is  
309 Arg65, which is surrounded by residues with a number of contacts below average between 0.5  
310 and 1.0. This rationalizes why  $R_2$  of Arg65 shows a local maximum that is still lower than  $R_2$  in  
311 other regions of p53TAD, such as residues 19–26 forming a residue cluster with an intermediate  
312 number of contacts. Notably, the 11 N-terminal residues of p53TAD display a lower-than-  
313 average amount of contacts, which is consistent with low  $R_2$  values observed across all 10  
314 individual MD trajectories. When the same type of contact analysis is performed with side-chain  
315 atoms only, a similar behavior is observed with only a small, systematic reduction in contacts  
316 (**Fig. S3**) reflecting that the majority of medium- to long-range inter-residue contacts are made  
317 by side-chain atoms.

318 We also grouped the number of contacts per snapshot formed by each residue according  
319 to residue type and normalized them by the number of residues of the same type. The resulting  
320 value for each amino acid residue type present in p53TAD and Pup reflects their inherent contact  
321 propensity (**Fig. 5C,D**). These profiles display the following trends: positively charged residues  
322 arginine and lysine are on average most prone to form contacts, followed by hydrophobic  
323 residues isoleucine and leucine as well as aromatic residues tryptophan and phenylalanine.  
324 Negatively charged residues aspartate and glutamate, however, are least disposed to form  
325 contacts. This may be also a consequence that both IDPs are overall negatively charged ( $-14e$  for  
326 p53TAD and  $-12e$  for Pup). When acidic residues outnumber basic residues, the former tend to  
327 repulse each other, thereby increasing  $R_g$ , while the latter have more options to interact with an

328 acidic residue than vice versa leading to an increase of the contact propensity of basic over acidic  
 329 residues.

330



331

332 **Fig. 5.** Number of close contacts formed by each residue during MD simulations of p53TAD and  
 333 Pup (without outliers) along with average residue-type specific contact propensities. For each  
 334 residue, the number of contacts was normalized by the number of snapshots for (A) p53TAD and  
 335 (B) Pup. Residues with their number of contacts per snapshot below 0.5 are depicted in blue,  
 336 0.5–1.5 in black, 1.5–2 in yellow, and above 2 in red. Primary sequences of p53TAD and Pup are  
 337 given at the bottom and colored as in Panels A, B. Average contact propensities according to  
 338 amino-acid residue type, which is the number of contacts per snapshot averaged over all residues  
 339 of the same type, are shown for (C) p53TAD, (D) Pup. Error bars correspond to the standard  
 340 deviations among different residues of the same type.



341 **Contact analysis by graph theory.** To investigate the nature of some of the most frequent  
342 pairwise contacts in these IDPs, the MD snapshots were analyzed by graph theory where each  
343 snapshot is represented as an undirected graph with each residue corresponding to an edge and  
344 an inter-residue contact corresponds to an edge connecting the two residues (nodes). The  
345 resulting graphs were then analyzed in terms of clusters, which are disconnected graph  
346 components that do not have any edges to nodes outside of the cluster. On average 6.0 clusters  
347 per snapshot are found for p53TAD and 5.4 clusters for Pup. The probabilities of a cluster to  
348 have a given size are represented for both IDPs by the histograms of cluster sizes (**Fig. 6A**),  
349 which reveal that clusters consisting of 2 nodes are most abundantly present (around 40%) in  
350 both p53TAD and Pup. Moreover, the cluster size probability decreases rapidly with increasing  
351 size. For instance, the fraction of clusters with 10 or more nodes (residues) is only 2–3%. Despite  
352 their sequence independence and different lengths, the two IDPs have strikingly similar cluster  
353 size distributions. The number of edges grows on average linearly with the number nodes  
354 (straight solid line), which is much slower than the quadratic behavior of complete graphs  
355 (dashed line, **Fig. 6B**). In fact, most of the clusters formed during MD simulations are sparse  
356 graphs with a relatively small average edge-to-node ratio of 1.54, which is indicative of tree-like  
357 graphs consisting mostly of linear branches with few cross-links. **Fig. 6** also depicts residue  
358 clusters (on the right) where pairwise contacts with occupancies  $> 0.2$  are depicted as an edge  
359 connecting two nodes (residues) with edge widths proportional to the pairwise contact  
360 occupancies.

361 The graph-theoretical representation of the transient interaction network uncovers the  
362 relationship between  $R_2$  profiles and transient contact formation and the types of interactions that  
363 are prevalent in IDP structures. For p53TAD, the three centers in the sequence with an elevated  
364 experimental  $R_2$  profile are (1) Lys24, (2) Glu51, and (3) Met66, and they are involved in or are  
365 sequentially adjacent to clusters A1, A3, and A2, respectively. Electrostatic interactions are  
366 important for residue cluster formation in p53TAD, in particular in cluster A2 featuring the  
367 pairwise contacts Lys65–Asp57 and Arg65–Glu62. The largest elevation of  $R_2$ , however, is the  
368 result of the largest interaction network A1. Hydrophobic and aromatic residues Phe19, Leu22,  
369 Trp23, Leu25 and Leu26 belong to a p53TAD segment that displays increased helical  
370 propensity(64, 65) (secondary structure propensities determined from chemical shifts are shown  
371 in **Fig. S5**) and which undergoes distinct loop closure dynamics.(66) In particular, residues

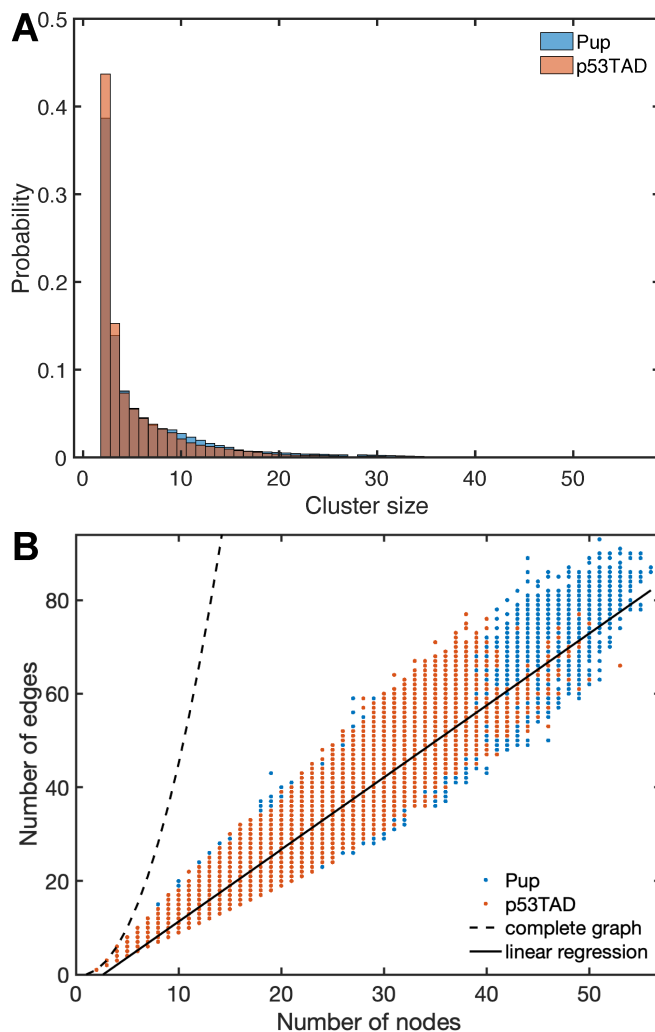
372 Phe19, Trp23, and Leu26 form the hydrophobic triad that is crucial for the binding of p53TAD to  
373 MDM2.(65) Similar to cluster A1, the smaller cluster A3 centered around Ile50 is also driven by  
374 hydrophobic interactions.

375 The regions of Pup with elevated  $R_2$  values (**Fig. 3D**) around Arg8, Ile18, Thr22, Arg29,  
376 Arg56 are all involved in clusters B1, B4, or B3 (**Fig. 4E,F**). Separate clusters can involve  
377 sequentially adjacent residues, such as clusters B2 and B3 or clusters B3 and B5 and thereby  
378 mediate cooperative behavior. The most dominant inter-residue interaction in Pup is of  
379 electrostatic nature resulting in the transient formation of salt bridges involving residue pairs in  
380 cluster B1.2 (Arg8–Asp14, Arg8–Asp15) and cluster B3 (Arg56–Asp53, Arg56–Glu52). Many of  
381 these residues appear to play the role of hubs promoting enhanced interactions also with other  
382 residues as visualized by the graphs in **Fig. 4E,F**.

383

384

385



386

387 **Fig. 6.** Graph theoretical analysis of inter-residual interactions and transient interaction networks  
388 of p53TAD and Pup. (A) Clusters consisting of 2 nodes (residues) dominate in the MD structures  
389 of p53TAD and Pup (without outlier trajectories), followed by clusters of size 3, etc. (B) The  
390 majority of the unique clusters are sparse graphs, with their number of edges much smaller than  
391 the number of edges in complete graphs growing with  $N(N-1)/2$  where  $N$  is the number of nodes.  
392 The average edge-to-node ratio is 1.54 (slope indicated by solid black line), indicating  
393 predominantly tree-like graphs that sometimes have a few additional edges (cross-linked  
394 branches).

395

396

## 397 DISCUSSION

398 Disordered proteins play a prominent role in many regulatory processes using their unique  
399 malleability to interact with their targets. Details of conformational substates of IDPs and how  
400 they are shaped by the complex interplay of inter-residue interaction networks are currently  
401 poorly understood both experimentally and computationally. In this work, we showed how the  
402 latest advances in MD force fields and computational protocols allow the nearly quantitative  
403 prediction of the complex behavior of the two IDPs p53TAD and Pup, including their dynamics  
404 time scales from site-resolved NMR spin relaxation.

405 The global dimensions of IDPs can be experimentally characterized by SAXS providing  
406 information about their radius of gyration  $R_g$  for direct comparison with MD ensembles. For Pup,  
407  $\langle R_g \rangle$  from the 10 1- $\mu$ s MD simulations follows the power law of **Eq. 6** with a Flory exponent  $\nu$   
408 = 0.601, which closely mirrors the behaviour of a self-avoiding random coil ( $\nu = 0.598$ ). By  
409 contrast, p53TAD is more expanded with  $\nu = 0.624$ , which is consistent with previous  
410 experimental results reported for this protein.(67) Such behaviour could be the result of stronger  
411 repulsive intra-residual forces caused by a slightly higher negative net charge (-14e of p53TAD  
412 vs. -12e of Pup) and a high percentage of prolines (18% in p53TAD vs. none in Pup) known to  
413 increase extendedness.(68) The relatively high  $\nu$  values of both proteins suggest that their  
414 interactions with water solvent are highly favorable preventing the hydrophobic collapse of their  
415 polypeptide chains.

416 The 10 1- $\mu$ s MD trajectories allow extensive sampling of the radius of gyration over time  
417 and extract characteristic time scales from its autocorrelation function (**Fig. 1**). For both proteins,  
418 the time-correlation function follows in good approximation a biexponential decay with  
419 correlation times around 10 and 55 ns. Global distance fluctuations can be studied  
420 experimentally by nanosecond fluorescence correlation spectroscopy (nsFCS), which found for 8  
421 M urea denatured ubiquitin global reconfiguration times  $\tau_r$  in the range of 50–90 ns.(16) A  
422 nsFCS study of  $\alpha$ -synuclein, which is about twice as long in sequence as the IDPs studied here,  
423 identified two reconfigurational correlation times of  $\tau_{r1} = 23$  ns and  $\tau_{r2} = 136$  ns.(30) These  
424 correlation times are within a factor 2–3 of those found in the current study, although it should be

425 kept in mind that they report about a donor/acceptor pair, i.e. S42C/T92C in the case of  $\alpha$ -  
426 synuclein, rather than about  $R_g$ .

427 Heteronuclear  $^{15}\text{N}$  relaxation offers a complementary view of IDP dynamics.  
428 Longitudinal  $R_1$  and transverse  $R_2$  relaxation rates are caused by local spin interactions, namely  
429 the magnetic dipole-dipole coupling and chemical shielding anisotropy, and they reflect  
430 reorientational dynamics amplitudes and timescales due to local conformational fluctuations as  
431 well as longer-range reorientational motional modes of the order of an IDP's persistence length  
432 and beyond. Model-free analysis is not applicable to IDP relaxation data due to the absence of a  
433 well-conserved global rotational diffusion tensor as reference frame.(27) Instead, a residue-by-  
434 residue interpretation can be applied where the correlation function of each site is described as a  
435 multiexponential function of the type of **Eq. 8** with 6 exponential dynamics modes.(28, 50, 55,  
436 62, 69) The hierarchy of dynamics modes depicted in **Fig. 3** shows a broad distribution of time  
437 scales including rapid librational motions ( $< 100$  ps) and dominant low nanosecond motions,  
438 which sample the different local energy basins of backbone  $\phi, \psi$  dihedral angles. The slowest  
439 modes with time scales in the range of 3–20 ns represent predominantly collective segmental  
440 reorientational motions. A similar hierarchy of time scales has been observed by fluorescence  
441 depolarization kinetics measurements of  $\alpha$ -synuclein.(48) These collective motions involve  
442 medium to longer-range interactions between residues that can be elucidated by graph theoretical  
443 analysis of the MD trajectories described here. For Pup, many of these slower motional modes  
444 have correlation times around 3–4 ns whereas for p53TAD they are on average twice as large.  
445 For both proteins the three distinct bands of time scales are pervasive across their polypeptide  
446 sequence (**Fig. 3E,F**).

447 MD methodology has made great strides in recent years toward an increasingly  
448 realistic representation of disordered proteins.(26) Besides experimental scattering data,  
449 quantitative NMR has played a key role for the independent validation of MD ensembles.  
450 Because NMR spin relaxation parameters fully quantitatively reflect IDP dynamics at atomic-  
451 level resolution both in terms of motional amplitudes and time scales, their accurate reproduction  
452 by MD has been an important but also very challenging task. A recent comparison of commonly  
453 used MD force fields that do not use residue-specific backbone potentials showed for several  
454 IDPs significant force-field dependences with the best results obtained when the analysis was

455 restricted to average correlation functions of chunks of 10-ns subtrajectories.(56) The need to  
456 exclude slower time-scale motions, which are prominent in both experimental data and  
457 simulations (see for example **Fig. 3**), may reflect the lack of convergence due to limited  
458 sampling. Beneficial for all simulations was the improvement of the TIP4P-D water model over  
459 TIP3P preventing overly collapsed IDP ensembles, which is consistent with other computational  
460 studies.(38, 57) Because of the observed discrepancies between experiments and MD simulations,  
461 some studies applied *post factum* adjustments to the MD simulations in order to improve  
462 agreement, which include uniform or selective scaling of the MD time scale or correlation  
463 times(27-30) or the reweighting of sub-trajectories.(62) Here, we chose a different approach:  
464 rather than relying on *post factum* modifications, we use the residue-specific ff99SBnmr2 force  
465 field, which was specifically designed for the improved representation of IDPs without the need  
466 of any corrections.(57, 58) A correction-free MD approach has recently been reported for the  
467 intrinsically disordered SH4UD protein with the Amber ff03ws force field, which does not use  
468 residue-type independent backbone dihedral angle potentials, and no time-scale dependent data,  
469 such as NMR spin relaxation, were used for validation.(70) NMR chemical shifts were back-  
470 calculated using SHIFTX2,(71) which, besides 3D structural information, makes extensive use of  
471 protein sequence data. Here, we back-calculated NMR chemical shifts using PPM(72) (**Fig. S4**),  
472 which only uses the physical parametrization of chemical shifts with respect to 3D protein  
473 structure of each snapshot,(71) achieving very good agreement.

474 The close correspondence observed between experimental and computed  $^{15}\text{N}$  relaxation  
475  $R_1$  and  $R_2$  relaxation rates for both IDPs studied here (**Fig. 3**), without the need for *post factum*  
476 corrections, attests to the accuracy and robustness of the computational protocol used. It applies  
477 REMD for the generation of conformational ensembles belonging to different temperatures from  
478 which 10 representative structures at 300 K were randomly selected as starting structures for 1-  
479  $\mu\text{s}$  MD trajectories whereby all simulations made use of the ff99SBnmr2 force field and the  
480 TIP4P-D water model. MD-derived longitudinal  $^{15}\text{N}$   $R_1$  follow the shapes of the experimental  $R_1$   
481 profiles with a small tendency to underestimate the experimental  $^{15}\text{N}$   $R_1$  rates by 4–6% whereas  
482  $^{15}\text{N}$   $R_2$  relaxation rates overestimate the experimental values on average by 26% for Pup and  
483 34% for p53TAD. This level of agreement is significantly better than for previously reported  
484 comparisons of this type. It is possible to achieve additional improvement by removing 1–2 MD  
485 trajectories starting from the most compact initial structures, a strategy proposed in the ABSURD

486 method (**Fig. S3**). Although *post factum* modifications can provide better agreement with  
487 experiment, it is generally not obvious whether the altered ensembles are in fact consistent with a  
488 modified, physics-based force field. If such a connection can be established it will allow, in  
489 principle, the further improvement of force fields for applications also to other proteins. Indeed,  
490 the ff99SBnmr1 force field, which is the parent force field of ff99SBnmr2, was developed and  
491 optimized using this strategy by the systematic reweighting of MD snapshots based on many trial  
492 force fields using experimental NMR data of intact proteins.(73)

493 The good agreement of the MD simulation with experimental observables both motivates  
494 and justifies the analysis of other protein properties observed in the MD trajectories that are  
495 difficult to measure. This includes the analysis of transient inter-residue interactions. The  
496 molecular driving forces of these interactions are fundamentally similar to those of ordered  
497 proteins although average hydration properties may differ.(70) In contrast to ordered proteins,  
498 inter-residue interactions between non-sequential amino acids are short-lived. Therefore, the  
499 time-averaged interaction maps (**Fig. 4A,B**) offer only partial insights as they conceal the  
500 compositions and distributions of instantaneous interaction clusters. In fact, the relatively large  
501 network reflected by the average contact map contrasts the much smaller size of graphs that exist  
502 at any given time, which attests to the very heterogeneous and transient nature of instantaneous  
503 contact clusters. The highest occupancy of pairwise contacts found is around 0.5, which mostly  
504 belong to  $(i,i+3)$  contacts. For a list of the most frequent pairwise contacts, see **Tables S2, S3**.

505 Snapshot by snapshot analysis revealed the dominance of small cluster sizes over larger  
506 ones (**Fig. 6**). For both p53TAD and Pup, clusters with 2 or 3 residues make up more than 50%  
507 of all clusters and clusters with more than 10 residues have notably low occurrence, although  
508 their formation could be functionally relevant during molecular recognition events. Because  
509 clusters consisting of residue pairs dominate intra-residual interactions in both IDPs, further  
510 analysis of the interaction network was performed based on pairwise contacts. Contact maps  
511 were generated for p53TAD and Pup averaged over all MD trajectories and pairwise contacts  
512 that have occupancies larger than 0.2 visualized as separate graphs (**Fig. 4E,F**). Instantaneous  
513 clusters can belong to such larger graphs as exemplified by clusters A1.1, A1.2, A1.3 for  
514 p53TAD and clusters B1.1 and B1.2 for Pup (**Fig. 4E,F**). The dominant clusters are  
515 characterized by a mix of hydrogen bonds, salt bridges (e.g., involving Arg65 in cluster A2,  
516 Arg8 in star-like cluster B1.2, and Arg56 in cluster B3), hydrophobic and aromatic interactions



517 (e.g., Phe19, Leu22/25/26, and Trp23 in cluster A1). These are consistent with the driving forces  
518 attributed to liquid-liquid phase separation, namely intermolecular contacts among aromatic  
519 residues,(74-76) electrostatic interactions,(77-79) and hydrophobic interactions.(80)

520 The majority of clusters are linear graphs with few circular sub-graphs leading to the  
521 linear relationship between the number of nodes and number of edges (**Fig. 6B**). Acidic residues  
522 tend to have low cluster participation whereas arginine residues have the highest participation in  
523 both proteins (**Fig. 5A,B**). This difference in cluster participation between cationic and anionic  
524 residues is also evident in **Fig. 5C,D**. Among the neutral amino acids, those with larger side-  
525 chains are more prone to interactions with non-neighboring residues due to their intrinsically  
526 larger distance range. In fact, Pro, Val, Ser, Ala, Gly have the lowest interaction propensities  
527 among neutral residues and among pairs of chemically similar residues, such as Gln vs. Asn and  
528 Leu vs. Val, the larger residue (Gln, Leu) dominates the smaller one (Asn, Val).

529 A primary biological function of p53TAD is to negatively regulate p53 by interacting  
530 with the ubiquitin ligases MDM2 and MDMX for the degradation of p53. This interaction is one  
531 of the earliest and best studied interactions between an IDP and a folded protein both by  
532 experiment(65, 66, 81) and computation.(82) In order to better understand the molecular  
533 recognition mechanism underlying the formation of this complex, a realistic and accurate  
534 description of the free state of p53TAD is of central importance. For MD studies, the choice of  
535 the protocol, especially of the force field and water model, is consequential. A recent unbiased  
536 REMD study of free p53TAD reported the detailed comparison using five different MD force  
537 fields all without residue-specific backbone potentials. Based on 1- $\mu$ s long replicas major  
538 differences were revealed in terms of the structural propensities among them and also with  
539 respect to experimental data.(83) An even longer simulation of residues 10–39 of p53TAD for a  
540 total length of 1.4 ms analyzed by Markov state models identified substantial populations of  $\beta$ -  
541 sheets across the sequence,(84) a behavior that is at variance with the above mentioned REMD  
542 ensembles(83) as well as with experimental solution NMR data.(65) These together with many  
543 other studies show that force fields need to be chosen following extensive testing to ensure that  
544 long trajectories, generated with considerable computational effort, offer the most realistic  
545 biophysical insights about these highly complex, heterogeneous systems.



546 In addition to forming transient intramolecular contacts, IDPs can also dynamically  
547 interact with other IDPs driving the formation of liquid-liquid phase separation. With a rapidly  
548 increasing body of experimental data on LLPS condensates,(9, 10, 85) all-atom MD simulations  
549 have an important role to play for a mechanistic understanding of emerging phase separation  
550 properties. Since the molecular driving forces of LLPS are the same as for intramolecular IDP  
551 interactions,(86) such as those described here, the optimal accuracy of force fields along with  
552 adequate sampling schemes of the heterogeneous condensate environment will be key for the  
553 quantitative interpretation of experimental data, allowing the prediction of condensate formation  
554 and eventually may open the way for new interventional approaches to actively reprogram  
555 condensates and their properties.

556 Although a possible role of Pup in LLPS is not known, LLPS involving full-length p53  
557 has been documented and p53TAD has been implicated in both phase separation and oncogenic  
558 amyloid aggregation.(87, 88) Multivalent electrostatic interactions between the N-terminal  
559 domain, p53TAD, and the C-terminal domain were identified as critical for LLPS, which were  
560 shown to be positively modulated through molecular crowding and negatively modulated by the  
561 addition of DNA and ATP molecules and post-translational modification. It was suggested that  
562 compartmentalization of p53 into the droplets suppresses its transcriptional regulatory function,  
563 while its release from droplets under cellular stress can activate p53.(87) These findings point to  
564 the need for the comprehensive characterization of these intermolecular interactions at residue-  
565 and atomic-level resolution. The agreement with experiment reported here clearly suggests that  
566 MD methodology has reached a level of accuracy allowing it to make critical contributions  
567 toward this goal.

568 The results of our study further advance the long-held premise of MD simulations to  
569 realistically describe IDP ensembles on their native dynamics time scales toward the better  
570 understanding of their biophysical properties and biological function. For the two IDPs p53TAD  
571 and Pup, the use of REMD allows the adequate sampling of conformational space for the  
572 generation of a representative set of initial structures that are then subjected to long, continuous  
573 MD simulations. The close agreement found for the extendedness of the simulated IDPs with  
574 experiment and polymer theory suggests an appropriate balance between the ff99SBnmr2 force  
575 field and the TIP4P-D water model at the global scale. It favorably complements the authentic  
576 IDP behavior achieved by this protocol on the local scale in terms of its compliance at the

577 individual residue level with coil libraries, scalar couplings, and chemical shifts. In addition to  
578 the realistic modeling of ensemble properties, our protocol also reproduces motional amplitudes  
579 and time scales encoded in quantitative NMR spin relaxation data with near experimental  
580 accuracy suggesting that the dominant minima of the free energy surface together with their  
581 many low-lying transition states are realistically captured by this comprehensive computational  
582 framework. These results prompted a more detailed analysis of short-lived inter-residue  
583 interactions, which was achieved by graph theory revealing characteristic inter-residue contact  
584 patterns and the extraction of residue-type specific interaction propensities. The realistic IDP  
585 conformational dynamics model achieved by the protocol described here advances our  
586 increasingly mechanistic and predictive understanding of IDPs along with their interactions and  
587 binding properties with ordered and disordered molecular targets ranging from regulatory  
588 pathways to emerging LLPS phenomena.

## 589 **METHODS**

590 **Molecular dynamics simulations.** Fully extended structures of p53TAD and Pup were prepared  
591 using the LEaP program in AmberTools16.(89) After equilibration, they were used to run  
592 replica-exchange MD (REMD) simulations for the sampling of conformational space (36  
593 replicas for each IDP covering a temperature range from 298–353 K for p53TAD and 298–365 K  
594 for Pup, see Supplementary Material) with each replica being 1  $\mu$ s of length. Exchange was  
595 attempted every 10 ps and the exchange probability was about 0.3. For each IDP, 10 structures  
596 were randomly selected from the room-temperature (298 K) REMD ensemble and used as initial  
597 structures to run free MD simulations for 1  $\mu$ s in the NPT ensemble at 300 K and 1 atm. The  
598 protein force field and water model used in all simulations were AMBER ff99SBnmr2 and  
599 TIP4P-D.

600 All MD simulations were performed using the GROMACS 2020.2 package.(90) The  
601 integration time step was set to 2 fs with all bond lengths containing hydrogen atoms constrained  
602 by the LINCS algorithm. Na<sup>+</sup> or Cl<sup>-</sup> ions were added to neutralize the total charge of the system.  
603 A 10 Å cutoff was used for all van der Waals and electrostatic interactions. Particle-mesh Ewald  
604 summation with a grid spacing of 1.2 Å was used to calculate long-range electrostatic  
605 interactions. A cubic simulation box extending 8 Å from the protein surface in all three

606 dimensions was used. Energy minimization was performed using the steepest descent algorithm  
 607 for 50,000 steps. The system was simulated for 100 ps at constant temperature and constant  
 608 volume with all protein heavy atoms positionally fixed. The pressure was then coupled to 1 atm  
 609 and the system was simulated for another 100 ps. The final production run of 1  $\mu$ s length was  
 610 performed in the NPT ensemble at 300 K and 1 atm. For simulation details, see **Table S1**.

611 **Radius of gyration tensor calculations and derived quantities.** In order to map the global  
 612 shape of p53TAD and Pup conformers, radius of gyration tensors were computed as 3 $\times$ 3  
 613 matrices  $\mathbf{S}$  from each snapshot of the room-temperature REMD ensemble and the free MD  
 614 simulations as follows:(91)

$$615 \quad S_{\alpha\beta} = \frac{1}{2N^2} \sum_{i,j=1}^N (r_{\alpha}^{(i)} - r_{\alpha}^{(j)})(r_{\beta}^{(i)} - r_{\beta}^{(j)}) \quad (2)$$

616 where  $r_{\alpha(\beta)}^{(i)}$  is cartesian coordinate  $\alpha$  ( $\beta$ ) (=  $x$ ,  $y$ ,  $z$ ) of atom  $i$  in the coordinate system that has its  
 617 origin in the center of mass of the molecule. Diagonalization of  $\mathbf{S}$  yields three non-negative  
 618 eigenvalues  $0 \leq \lambda_1 \leq \lambda_2 \leq \lambda_3$  from which the *radius of gyration*  $R_g$  is obtained,  $R_g = (\lambda_1 + \lambda_2 + \lambda_3)^{1/2}$ ,  
 619 the *asphericity*  $A$ ,(91, 92)

$$620 \quad A = \frac{(\lambda_3 - \lambda_2)^2 + (\lambda_3 - \lambda_1)^2 + (\lambda_2 - \lambda_1)^2}{2(\lambda_3 + \lambda_2 + \lambda_1)^2} \quad (3)$$

621 and the *prolateness*  $P$ ,(93)

$$622 \quad P = \frac{(2\lambda_3 - \lambda_2 - \lambda_1)(2\lambda_2 - \lambda_3 - \lambda_1)(2\lambda_1 - \lambda_3 - \lambda_2)}{2(\lambda_3^2 + \lambda_2^2 + \lambda_1^2 - \lambda_3\lambda_2 - \lambda_3\lambda_1 - \lambda_2\lambda_1)^{3/2}} \quad (4)$$

623 The asphericity measures the degree to which the three axis lengths of the ellipsoid of inertia  
 624 (eigenvalues) are equal, whereas the prolateness  $P$  indicates whether the largest or smallest axis  
 625 length is closer to the middle axis length.  $P$  takes values between -1 and 1, quantifying the  
 626 transition from oblate to prolate shapes. Normalized time-correlation functions of  $R_g(t)$ , made  
 627 offset-free, were computed according to

$$628 \quad C_{R_g}(t) = \langle (R_g(\tau) - \langle R_g \rangle)(R_g(t+\tau) - \langle R_g \rangle) \rangle_{\tau} / \langle (R_g(\tau) - \langle R_g \rangle)^2 \rangle_{\tau} \quad (5)$$

629 as an average over all 1- $\mu$ s MD trajectories.

630 According to polymer theory, for an unfolded polymer the ensemble-averaged  $R_g$  scales  
631 with the number of residues  $N$  as(61)

$$632 \quad \langle R_g \rangle = \rho_0 N^\nu \quad (6)$$

633 where  $\rho_0$  is a constant reflecting the average size of a residue and the Flory exponent  
634  $\nu$  determines the overall compactness of the polymer serving as a reference.

635 **Back-calculation of  $R_1$ ,  $R_2$  relaxation rates.** For IDPs, the normalized time-autocorrelation  
636 function  $C(t)$  of the lattice part of the spin-relaxation active magnetic dipole-dipole interaction  
637 cannot be factorized into an overall tumbling part and an internal dynamics part. Rather, we  
638 compute the full  $C(t)$  directly from an MD trajectory using the second-order Legendre  
639 polynomial:

$$640 \quad C(t) = \frac{1}{2} \langle 3[\mathbf{e}(\tau)\mathbf{e}(\tau + t)]^2 - 1 \rangle \quad (7)$$

641 where  $\mathbf{e}(t)$  is the unit vector defining the  $^{15}\text{N}$ - $^1\text{H}$  bond orientation whereby snapshots were *not*  
642 aligned with respect to a reference snapshot. The angular brackets indicate averaging from time  $\tau$   
643 = 0 to  $T_{\text{MD}} - t$ , where  $T_{\text{MD}}$  is the total trajectory length. The calculation of  $C(t)$  was efficiently  
644 performed by the fast Fourier transform (FFT) using the Wiener-Khinchin theorem. For  
645 acceptable statistical convergence, the analysis of  $C(t)$  was limited to its initial portion from  $t = 0$   
646 -  $T_{\text{MD}}/3$ . Next, a multiexponential decay function was fitted to  $C(t)$ :(94)

$$647 \quad C(t) = \sum_{i=1}^6 A_i e^{-t/\tau_i} \quad (8)$$

648 where  $A_i$  and  $\tau_i$  are the best fitting parameters subject to the conditions:

$$649 \quad \sum_{i=1}^6 A_i = 1 \quad A_i \geq 0, \tau_i \geq 0 \quad (9)$$

650 The spectral density function  $J(\omega)$  can be then analytically obtained via Fourier transformation of  
651  $C(t)$ :

$$652 \quad J(\omega) = 2 \int_0^\infty C(t) \cos(\omega t) dt = \sum_{i=1}^6 \frac{2A_i \tau_i}{1 + (\omega \tau_i)^2} \quad (10)$$

653 NMR spin relaxation parameters  $R_1$  and  $R_2$  were then computed using the standard  
654 expressions:(95-98)

$$655 \quad R_1 = d_{00}[3J(\omega_N) + J(\omega_H - \omega_N) + 6J(\omega_H + \omega_N)] + c_{00}\omega_N^2 J(\omega_N) \quad (11)$$

$$656 \quad R_2 = \frac{1}{2}d_{00}[4J(0) + 3J(\omega_N) + J(\omega_H - \omega_N) + 6J(\omega_H) + 6J(\omega_H + \omega_N)] + \frac{1}{6}c_{00}\omega_N^2[4J(0) +$$
$$657 \quad 3J(\omega_N)] \quad (12)$$

658 where  $d_{00} = \frac{1}{20}(\frac{\mu_0}{4\pi})^2(\frac{h}{2\pi})^2\gamma_H^2\gamma_N^2\langle r_{NH}^{-3} \rangle^2$  and  $c_{00} = \frac{1}{15}\Delta\sigma^2$ .  $\mu_0$  is the permeability of vacuum,  $h$  is  
659 Plank's constant,  $\gamma_H$  and  $\gamma_N$  are the gyromagnetic ratios of  $^1H$  and  $^{15}N$ , and  $r_{NH} = 1.02 \text{ \AA}$  is the  
660 backbone N-H bond length. The  $^{15}N$  chemical shift anisotropy was set to  $\Delta\sigma = -160$  ppm.

661 **Analysis of inter-residue contacts and residue clusters by graph theory.** Contact analysis was  
662 performed on all snapshots of the MD simulations of both p53TAD and Pup. A contact is  
663 considered formed when the nearest distance between atoms from two different residues is  
664 smaller than 4  $\text{\AA}$ . First-neighbor contacts (between residues  $i,i+1$ ), and second-neighbor contacts  
665 (between residues  $i,i+2$ ) were excluded since they are present for most residues. For each residue  
666 in p53TAD and Pup, the total number of contacts formed by a particular residue is determined  
667 and normalized by the number of MD snapshots. Each snapshot was converted to a graph where  
668 residues are represented as nodes and contacts between two residues are represented as edges  
669 between them. The initial graph was then decomposed into a maximal number of disconnected  
670 graph components called *clusters*, i.e. there is no edge between any node in the cluster and any  
671 node outside the cluster. The size of a cluster corresponds to the number of its nodes.

672

## 673 ACKNOWLEDGEMENTS

674 We thank Dr. Da-Wei Li for helping with the graph theoretical analysis. MD and REMD  
675 simulations were performed at the Ohio Supercomputer Center. The authors declare that they  
676 have no competing interests. All data needed to evaluate the conclusions in the paper are present  
677 in the paper and/or the Supporting Information.

## 678 SUPPORTING INFORMATION

679 Fig. S1. Radius of gyration of the IDPs p53TAD and Pup in 10 1- $\mu$ s MD trajectories each at 300  
680 K with starting structures randomly chosen from replica exchange simulations.

681 Fig. S2. Mean  $R_1$ ,  $R_2$  errors from 10 1- $\mu$ s MD simulations of p53TAD and Pup in comparison  
682 with experiment.

683 Fig. S3. Back-calculated  $R_1$ ,  $R_2$   $^{15}\text{N}$  backbone spin relaxation rates from microsecond MD  
684 simulations of p53TAD and Pup excluding atypical trajectories in comparison with experiment.

685 Fig. S4. Comparisons of experimental and predicted chemical shifts of p53TAD.

686 Fig. S5. Experimental and MD-derived secondary structure propensities of p53TAD.

687 Fig. S6. Average number of contacts formed by a particular residue in p53TAD and Pup per  
688 snapshot using only side-chain atoms.

689 Fig. S7. Contact propensities according to amino-acid residue type for both proteins combined.

690 Table S1. MD and REMD simulation details for p53TAD and Pup.

691 Table S2. Most frequent pairwise residue contacts in p53TAD from MD simulations.

692 Table S3. Most frequent pairwise residue contacts in Pup from MD simulations.

693

## 694 REFERENCES

- 695 1. Wright PE, Dyson HJ. Intrinsically disordered proteins in cellular signalling and regulation. *Nat Rev*  
696 *Mol Cell Bio.* 2015;16(1):18-29.
- 697 2. Habchi J, Tompa P, Longhi S, Uversky VN. Introducing Protein Intrinsic Disorder. *Chem Rev.*  
698 2014;114(13):6561-88.
- 699 3. Tompa P. Unstructural biology coming of age. *Curr Opin Struct Biol.* 2011;21(3):419-25.
- 700 4. Uversky VN, Oldfield CJ, Dunker AK. Intrinsically Disordered Proteins in Human Diseases:  
701 Introducing the D2 Concept. *Annu Rev Biophys.* 2008;37:215-46.
- 702 5. van der Lee R, Buljan M, Lang B, Weatheritt RJ, Daughdrill GW, Dunker AK, et al. Classification of  
703 Intrinsically Disordered Regions and Proteins. *Chem Rev.* 2014;114(13):6589-631.
- 704 6. Romer L, Klein C, Dehner A, Kessler H, Buchner J. p53 - A natural cancer killer: Structural insights  
705 and therapeutic concepts. *Angew Chem Int Edit.* 2006;45(39):6440-60.
- 706 7. Chen X, Solomon WC, Kang Y, Cerda-Maira F, Darwin KH, Walters KJ. Prokaryotic Ubiquitin-Like  
707 Protein Pup Is Intrinsically Disordered. *J Mol Bio.* 2009;392(1):208-17.
- 708 8. Alberti S, Gladfelter A, Mittag T. Considerations and Challenges in Studying Liquid-Liquid Phase  
709 Separation and Biomolecular Condensates. *Cell.* 2019;176(3):419-34.
- 710 9. Banani SF, Lee HO, Hyman AA, Rosen MK. Biomolecular condensates: organizers of cellular  
711 biochemistry. *Nat Rev Mol Cell Bio.* 2017;18(5):285-98.
- 712 10. Shin Y, Brangwynne CP. Liquid phase condensation in cell physiology and disease. *Science.*  
713 2017;357(6357).
- 714 11. Uversky VN. Intrinsically disordered proteins in overcrowded milieu: Membrane-less organelles,  
715 phase separation, and intrinsic disorder. *Curr Opin Struct Biol.* 2017;44:18-30.
- 716 12. Sormanni P, Piovesan D, Heller GT, Bonomi M, Kukic P, Camilloni C, et al. Simultaneous  
717 quantification of protein order and disorder. *Nat Chem Biol.* 2017;13(4):339-42.
- 718 13. Ozenne V, Bauer F, Salmon L, Huang JR, Jensen MR, Segard S, et al. Flexible-meccano: a tool for the  
719 generation of explicit ensemble descriptions of intrinsically disordered proteins and their  
720 associated experimental observables. *Bioinformatics.* 2012;28(11):1463-70.
- 721 14. Marsh JA, Forman-Kay JD. Ensemble modeling of protein disordered states: Experimental restraint  
722 contributions and validation. *Proteins.* 2012;80(2):556-72.
- 723 15. Jensen MR, Zweckstetter M, Huang JR, Backledge M. Exploring Free-Energy Landscapes of  
724 Intrinsically Disordered Proteins at Atomic Resolution Using NMR Spectroscopy. *Chem Rev.*  
725 2014;114(13):6632-60.
- 726 16. Aznauryan M, Delgado L, Soranno A, Nettels D, Huang JR, Labhardt AM, et al. Comprehensive  
727 structural and dynamical view of an unfolded protein from the combination of single-molecule  
728 FRET, NMR, and SAXS. *Proc Natl Acad Sci USA.* 2016;113(37):E5389-E98.
- 729 17. Gomes GNW, Krzeminski M, Namini A, Martin EW, Mittag T, Head-Gordon T, et al. Conformational  
730 Ensembles of an Intrinsically Disordered Protein Consistent with NMR, SAXS, and Single-Molecule  
731 FRET. *J Am Chem Soc.* 2020;142(37):15697-710.
- 732 18. Wang WN. Recent advances in atomic molecular dynamics simulation of intrinsically disordered  
733 proteins. *Phys Chem Chem Phys.* 2021;23(2):777-84.
- 734 19. Pitera JW, Chodera JD. On the Use of Experimental Observations to Bias Simulated Ensembles. *J*  
735 *Chem Theory Comput.* 2012;8(10):3445-51.



- 736 20. Roux B, Weare J. On the statistical equivalence of restrained-ensemble simulations with the  
737 maximum entropy method. *J Chem Phys.* 2013;138(8).
- 738 21. Cavalli A, Camilloni C, Vendruscolo M. Molecular dynamics simulations with replica-averaged  
739 structural restraints generate structural ensembles according to the maximum entropy principle. *J*  
740 *Chem Phys.* 2013;138(9).
- 741 22. Camilloni C, Vendruscolo M. Statistical Mechanics of the Denatured State of a Protein Using  
742 Replica-Averaged Metadynamics. *J Am Chem Soc.* 2014;136(25):8982-91.
- 743 23. Hummer G, Koefinger J. Bayesian ensemble refinement by replica simulations and reweighting. *J*  
744 *Chem Phys.* 2015;143(24).
- 745 24. Salvi N, Abyzov A, Blackledge M. Multi-Timescale Dynamics in Intrinsically Disordered Proteins from  
746 NMR Relaxation and Molecular Simulation. *J Phys Chem Lett.* 2016;7(13):2483-9.
- 747 25. Cheng P, Peng JH, Zhang ZY. SAXS-Oriented Ensemble Refinement of Flexible Biomolecules. *Biophys*  
748 *J.* 2017;112(7):1295-301.
- 749 26. Best RB. Computational and theoretical advances in studies of intrinsically disordered proteins.  
750 *Curr Opin Struct Biol.* 2017;42:147-54.
- 751 27. Prompers JJ, Brüschweiler R. General Framework for Studying the Dynamics of Folded and  
752 Nonfolded Proteins by NMR Relaxation Spectroscopy and MD Simulation. *J Am Chem Soc.*  
753 2002;124(16):4522-34.
- 754 28. Xue Y, Skrynnikov NR. Motion of a Disordered Polypeptide Chain as Studied by Paramagnetic  
755 Relaxation Enhancements, N-15 Relaxation, and Molecular Dynamics Simulations: How Fast Is  
756 Segmental Diffusion in Denatured Ubiquitin? *J Am Chem Soc.* 2011;133(37):14614-28.
- 757 29. Rezaei-Ghaleh N, Parigi G, Zweckstetter M. Reorientational Dynamics of Amyloid- $\beta$  from NMR Spin  
758 Relaxation and Molecular Simulation. *J Phys Chem Lett.* 2019;10(12):3369-75.
- 759 30. Rezaei-Ghaleh N, Parigi G, Soranno A, Holla A, Becker S, Schuler B, et al. Local and Global Dynamics  
760 in Intrinsically Disordered Synuclein. *Angew Chem Int Edit.* 2018;57(46):15262-6.
- 761 31. Ahmed MC, Skaanning LK, Jussupow A, Newcombe EA, Kragelund BB, Camilloni C, et al. Refinement  
762 of  $\alpha$ -Synuclein Ensembles Against SAXS Data: Comparison of Force Fields and Methods. *Front Mol*  
763 *Biosci.* 2021;8.
- 764 32. Maier JA, Martinez C, Kasavajhala K, Wickstrom L, Hauser KE, Simmerling C. ff14SB: Improving the  
765 Accuracy of Protein Side Chain and Backbone Parameters from ff99SB. *J Chem Theory Comput.*  
766 2015;11(8):3696-713.
- 767 33. Tian C, Kasavajhala K, Belfon KAA, Raguette L, Huang H, Migués AN, et al. ff19SB: Amino-Acid-  
768 Specific Protein Backbone Parameters Trained against Quantum Mechanics Energy Surfaces in  
769 Solution. *J Chem Theory Comput.* 2020;16(1):528-52.
- 770 34. Huang J, Rauscher S, Nawrocki G, Ran T, Feig M, de Groot BL, et al. CHARMM36m: an improved  
771 force field for folded and intrinsically disordered proteins. *Nat Methods.* 2017;14(1):71-3.
- 772 35. Robustelli P, Piana S, Shaw DE. Developing a molecular dynamics force field for both folded and  
773 disordered protein states. *Proc Natl Acad Sci USA.* 2018;115(21):E4758-E66.
- 774 36. Best RB, Zheng W, Mittal J. Balanced Protein-Water Interactions Improve Properties of Disordered  
775 Proteins and Non-Specific Protein Association. *J Chem Theory Comput.* 2014;10(11):5113-24.
- 776 37. Nerenberg PS, Head-Gordon T. Optimizing Protein-Solvent Force Fields to Reproduce Intrinsic  
777 Conformational Preferences of Model Peptides. *J Chem Theory Comput.* 2011;7(4):1220-30.
- 778 38. Piana S, Donchev AG, Robustelli P, Shaw DE. Water Dispersion Interactions Strongly Influence  
779 Simulated Structural Properties of Disordered Protein States. *J Phys Chem B.* 2015;119(16):5113-23.



- 780 39. Izadi S, Anandkrishnan R, Onufriev AV. Building Water Models: A Different Approach. *J Phys Chem*  
781 *Lett.* 2014;5(21):3863-71.
- 782 40. Mu J, Pan Z, Chen H-F. Balanced Solvent Model for Intrinsically Disordered and Ordered Proteins. *J*  
783 *Chem Inf Model.* 2021;61(10):5141-51.
- 784 41. Kang W, Jiang F, Wu YD. How to strike a conformational balance in protein force fields for  
785 molecular dynamics simulations? *Wires Comput Mol Sci.* 2021.
- 786 42. Song D, Luo R, Chen H-F. The IDP-Specific Force Field *ff14IDPSFF* Improves the Conformer Sampling  
787 of Intrinsically Disordered Proteins. *J Chem Inf Model.* 2017;57(5):1166-78.
- 788 43. Liu H, Song D, Lu H, Luo R, Chen H-F. Intrinsically disordered protein-specific force field  
789 CHARMM36IDPSFF. *Chem Biol Drug Des.* 2018;92(4):1722-35.
- 790 44. Song D, Liu H, Luo R, Chen H-F. Environment-Specific Force Field for Intrinsically Disordered and  
791 Ordered Proteins. *J Chem Inf Model.* 2020;60(4):2257-67.
- 792 45. Jiang F, Zhou C-Y, Wu Y-D. Residue-Specific Force Field Based on the Protein Coil Library. RSFF1:  
793 Modification of OPLS-AA/L. *J Phys Chem B.* 2014;118(25):6983-98.
- 794 46. Zhou C-Y, Jiang F, Wu Y-D. Residue-Specific Force Field Based on Protein Coil Library. RSFF2:  
795 Modification of AMBER ff99SB. *J Phys Chem B.* 2015;119(3):1035-47.
- 796 47. Kang W, Jiang F, Wu Y-D. Universal Implementation of a Residue-Specific Force Field Based on  
797 CMAP Potentials and Free Energy Decomposition. *J Chem Theory Comput.* 2018;14(8):4474-86.
- 798 48. Das D, Arora L, Mukhopadhyay S. Fluorescence Depolarization Kinetics Captures Short-Range  
799 Backbone Dihedral Rotations and Long-Range Correlated Dynamics of an Intrinsically Disordered  
800 Protein. *J Phys Chem B.* 2021;125(34):9708-18.
- 801 49. Alexandrescu AT, Shortle D. Backbone Dynamics of a Highly Disordered 131 Residue Fragment of  
802 Staphylococcal Nuclease. *J Mol Biol.* 1994;242(4):527-46.
- 803 50. Brutscher B, Brüschweiler R, Ernst RR. Backbone dynamics and structural characterization of the  
804 partially folded A state of ubiquitin by  $^1\text{H}$ ,  $^{13}\text{C}$ , and  $^{15}\text{N}$  nuclear magnetic resonance spectroscopy.  
805 *Biochemistry.* 1997;36(42):13043-53.
- 806 51. Schwalbe H, Fiebig KM, Buck M, Jones JA, Grimshaw SB, Spencer A, et al. Structural and Dynamical  
807 Properties of a Denatured Protein. Heteronuclear 3D NMR Experiments and Theoretical  
808 Simulations of Lysozyme in 8 M Urea. *Biochemistry.* 1997;36(29):8977-91.
- 809 52. Klein-Seetharaman J, Oikawa M, Grimshaw SB, Wirmer J, Duchardt E, Ueda T, et al. Long-Range  
810 Interactions Within a Nonnative Protein. *Science.* 2002;295(5560):1719-22.
- 811 53. Schwarzinger S, Wright PE, Dyson HJ. Molecular hinges in protein folding: The urea-denatured state  
812 of apomyoglobin. *Biochemistry.* 2002;41(42):12681-6.
- 813 54. Salvi N, Abyzov A, Blackledge M. Analytical Description of NMR Relaxation Highlights Correlated  
814 Dynamics in Intrinsically Disordered Proteins. *Angew Chem Int Edit.* 2017;56(45):14020-4.
- 815 55. Kampf K, Izmailov SA, Rabdano SO, Groves AT, Podkorytov IS, Skrynnikov NR. What Drives  $^{15}\text{N}$  Spin  
816 Relaxation in Disordered Proteins? Combined NMR/MD Study of the H4 Histone Tail. *Biophys J.*  
817 2018;115(12):2348-67.
- 818 56. Zapletal V, Mladek A, Melkova K, Lousa P, Nomilner E, Jasenakova Z, et al. Choice of Force Field for  
819 Proteins Containing Structured and Intrinsically Disordered Regions. *Biophys J.* 2020;118(7):1621-  
820 33.
- 821 57. Yu L, Li D-W, Bruschiweiler R. Balanced Amino-Acid-Specific Molecular Dynamics Force Field for the  
822 Realistic Simulation of Both Folded and Disordered Proteins. *J Chem Theory Comput.*  
823 2020;16(2):1311-8.

- 824 58. Yu L, Li D-W, Brüscheiler R. Systematic Differences between Current Molecular Dynamics Force  
825 Fields To Represent Local Properties of Intrinsically Disordered Proteins. *J Phys Chem B*.  
826 2021;125(3):798-804.
- 827 59. Le Guillou JC, Zinn-Justin J. Critical Exponents for the  $n$ -Vector Model in Three Dimensions from  
828 Field Theory. *Phys Rev Lett*. 1977;39(2):95-8.
- 829 60. Kohn JE, Millett IS, Jacob J, Zagrovic B, Dillon TM, Cingel N, et al. Random-coil behavior and the  
830 dimensions of chemically unfolded proteins. *Proc Natl Acad Sci USA*. 2004;101(34):12491-6.
- 831 61. Flory PJ. Principles of polymer chemistry. Ithaca,; Cornell University Press; 1953. 672 p.
- 832 62. Adamski W, Salvi N, Maurin D, Magnat J, Milles S, Jensen MR, et al. A Unified Description of  
833 Intrinsically Disordered Protein Dynamics under Physiological Conditions Using NMR Spectroscopy.  
834 *J Am Chem Soc*. 2019;141(44):17817-29.
- 835 63. Lienin SF, Brems T, Brutscher B, Brüscheiler R, Ernst RR. Anisotropic intramolecular backbone  
836 dynamics of ubiquitin characterized by NMR relaxation and MD computer simulation. *J Am Chem*  
837 *Soc*. 1998;120(38):9870-9.
- 838 64. Wong TS, Rajagopalan S, Freund SM, Rutherford TJ, Andreeva A, Townsley FM, et al. Biophysical  
839 characterizations of human mitochondrial transcription factor A and its binding to tumor  
840 suppressor p53. *Nucleic Acids Res*. 2009;37(20):6765-83.
- 841 65. Shan B, Li DW, Bruscheiler-Li L, Brüscheiler R. Competitive Binding between Dynamic p53  
842 Transactivation Subdomains to Human MDM2 Protein: implications for regulating the  
843 p53·MDM2/MDMX interaction. *J Biol Chem*. 2012;287(36):30376-84.
- 844 66. Lum JK, Neuweiler H, Fersht AR. Long-Range Modulation of Chain Motions within the Intrinsically  
845 Disordered Transactivation Domain of Tumor Suppressor p53. *J Am Chem Soc*. 2012;134(3):1617-  
846 22.
- 847 67. Daughdrill GW, Kashtanov S, Stancik A, Hill SE, Helms G, Muschol M, et al. Understanding the  
848 structural ensembles of a highly extended disordered protein. *Mol Biosyst*. 2012;8(1):308-19.
- 849 68. Marsh JA, Forman-Kay JD. Sequence Determinants of Compaction in Intrinsically Disordered  
850 Proteins. *Biophys J*. 2010;98(10):2383-90.
- 851 69. Prompers JJ, Scheurer C, Brüscheiler R. Characterization of NMR relaxation-active motions of a  
852 partially folded A-state analogue of ubiquitin. *J Mol Biol*. 2001;305(5):1085-97.
- 853 70. Shrestha UR, Juneja P, Zhang Q, Gurumoorthy V, Borreguero JM, Urban V, et al. Generation of the  
854 configurational ensemble of an intrinsically disordered protein from unbiased molecular dynamics  
855 simulation. *Proc Natl Acad Sci USA*. 2019;116(41):20446-52.
- 856 71. Xu XP, Case DA. Automated prediction of  $^{15}\text{N}$ ,  $^{13}\text{C}^\alpha$ ,  $^{13}\text{C}^\beta$  and  $^{13}\text{C}'$  chemical shifts in proteins using a  
857 density functional database. *J Biomol NMR*. 2001;21(4):321-33.
- 858 72. Li D-W, Brüscheiler R. PPM: a side-chain and backbone chemical shift predictor for the  
859 assessment of protein conformational ensembles. *J Biomol NMR*. 2012;54(3):257-65.
- 860 73. Li D-W, Brüscheiler R. NMR-based protein potentials. *Angew Chem Int Edit*. 2010;49(38):6778-80.
- 861 74. Brangwynne CP, Tompa P, Pappu RV. Polymer physics of intracellular phase transitions. *Nat Phys*.  
862 2015;11(11):899-904.
- 863 75. Nott TJ, Petsalaki E, Farber P, Jervis D, Fussner E, Plochowitz A, et al. Phase Transition of a  
864 Disordered Nuage Protein Generates Environmentally Responsive Membraneless Organelles. *Mol*  
865 *Cell*. 2015;57(5):936-47.
- 866 76. Vernon RM, Forman-Kay JD. First-generation predictors of biological protein phase separation. *Curr*  
867 *Opin Struct Biol*. 2019;58:88-96.

- 868 77. Elbaum-Garfinkle S, Kim Y, Szczepaniak K, Chen CCH, Eckmann CR, Myong S, et al. The disordered P  
869 granule protein LAF-1 drives phase separation into droplets with tunable viscosity and dynamics.  
870 Proc Natl Acad Sci USA. 2015;112(23):7189-94.
- 871 78. Tsang B, Arsenault J, Vernon RM, Lin H, Sonenberg N, Wang LY, et al. Phosphoregulated FMRP  
872 phase separation models activity-dependent translation through bidirectional control of mRNA  
873 granule formation. Proc Natl Acad Sci USA. 2019;116(10):4218-27.
- 874 79. Pak CW, Kosno M, Holehouse AS, Padrick SB, Mittal A, Ali R, et al. Sequence Determinants of  
875 Intracellular Phase Separation by Complex Coacervation of a Disordered Protein. Mol Cell.  
876 2016;63(1):72-85.
- 877 80. Reichheld SE, Muiznieks LD, Keeley FW, Sharpe S. Direct observation of structure and dynamics  
878 during phase separation of an elastomeric protein. Proc Natl Acad Sci USA. 2017;114(22):E4408-  
879 E15.
- 880 81. Kussie PH, Gorina S, Marechal V, Elenbaas B, Moreau J, Levine AJ, et al. Structure of the MDM2  
881 oncoprotein bound to the p53 tumor suppressor transactivation domain. Science.  
882 1996;274(5289):948-53.
- 883 82. Demir O, Barros EP, Offutt TL, Rosenfeld M, Amaro RE. An integrated view of p53 dynamics,  
884 function, and reactivation. Curr Opin Struct Biol. 2021;67:187-94.
- 885 83. Liu X, Chen J. Residual Structures and Transient Long-Range Interactions of p53 Transactivation  
886 Domain: Assessment of Explicit Solvent Protein Force Fields. J Chem Theory Comput.  
887 2019;15(8):4708-20.
- 888 84. Herrera-Nieto P, Perez A, De Fabritiis G. Characterization of partially ordered states in the  
889 intrinsically disordered N-terminal domain of p53 using millisecond molecular dynamics simulations.  
890 Sci Rep. 2020;10(1).
- 891 85. Alberti S, Dormann D. Liquid-Liquid Phase Separation in Disease. Annu Rev Genet. 2019;53:171-94.
- 892 86. Dignon GL, Best RB, Mittal J. Biomolecular Phase Separation: From Molecular Driving Forces to  
893 Macroscopic Properties. Annu Rev Phys Chem. 2020;71:53-75.
- 894 87. Kamagata K, Kanbayashi S, Honda M, Itoh Y, Takahashi H, Kameda T, et al. Liquid-like droplet  
895 formation by tumor suppressor p53 induced by multivalent electrostatic interactions between two  
896 disordered domains. Sci Rep. 2020;10(1).
- 897 88. Petronilho EC, Pedrote MM, Marques MA, Passos YM, Mota MF, Jakobus B, et al. Phase separation  
898 of p53 precedes aggregation and is affected by oncogenic mutations and ligands. Chem Sci.  
899 2021;12(21):7334-49.
- 900 89. Case DA, Betz RM, Cerutti DS, Cheatham III TE, Darden TA, Duke RE, et al. AMBER 2016. University  
901 of California, San Francisco. 2016.
- 902 90. Abraham MJ, Murtola T, Schulz R, Páll S, Smith JC, Hess B, et al. GROMACS: High performance  
903 molecular simulations through multi-level parallelism from laptops to supercomputers. SoftwareX.  
904 2015;1-2:19-25.
- 905 91. Rawdon EJ, Kern JC, Piatek M, Plunkett P, Stasiak A, Millett KC. Effect of Knotting on the Shape of  
906 Polymers. Macromolecules. 2008;41(21):8281-7.
- 907 92. Rudnick J, Gaspari G. The asphery of random walks. J Phys A. 1986;19(4):L191-L3.
- 908 93. Diehl HW, Eisenriegler E. Universal shape ratios for open and closed random walks: exact results for  
909 all  $d$ . J Phys A. 1989;22(3):L87-L91.

- 910 94. Brems T, Brüschweiler R, Ernst RR. A Protocol for the Interpretation of Side-Chain Dynamics Based  
911 on NMR Relaxation: Application to Phenylalanines in Antamanide. *J Am Chem Soc.*  
912 1997;119(18):4272-84.
- 913 95. Wangsness RK, Bloch F. The dynamical theory of nuclear induction. *Phys Rev.* 1953;89(4):728-39.
- 914 96. Bloch F. Dynamical theory of nuclear induction. II. *Phys Rev.* 1956;102(1):104-35.
- 915 97. Redfield AG. On the theory of relaxation processes. *Ibm J Res Dev.* 1957;1(1):19-31.
- 916 98. Abragam A. *The Principles of Nuclear Magnetism*: Clarendon Press; 1961.
- 917
- 918